RSC Advances

PAPER

View Article Online
View Journal | View Issue

Check for updates

Cite this: *RSC Adv.*, 2023, **13**, 16342

Methanol steam reforming for hydrogen production over $NiTiO_3$ nanocatalyst with hierarchical porous structure†

Qijie Jin,‡[ad] Xuelu Meng,‡[a] Peng Wu,[c] Yunhe Li,[a] Mutao Xu,[ab] Ranran Zhou,[a] Mengfei Yang[b] and Haitao Xu *[ad]

Received 2nd May 2023
Accepted 25th May 2023

DOI: 10.1039/d3ra02891g

rsc.li/rsc-advances

Steam reforming for hydrogen production is one of the important research directions for clean energy. $NiTiO_3$ catalysts with a hierarchical porous structure are prepared and applied to methanol steam reforming for hydrogen production. The results show that the optimum catalyst (10% Ni–Ti–O_x) not only has a hierarchical porous structure, but it also involves the coexistence of $NiTiO_3$, anatase TiO_2 and rutile TiO_2. The formation of $NiTiO_3$ is beneficial to the adsorption and activation of methanol molecules on the surface of the Ni–Ti–O_x catalyst, and the main intermediate species of the methanol molecular reaction are hydroxyl groups, methoxy species and formic acid species. Furthermore, the methanol steam reforming reaction is mainly dominated by methanol decomposition at low temperature (350–500 °C), while it is mainly dominated by methanol and water molecular reactions at high temperature (500–600 °C).

Open Access Article. Published on 31 May 2023. Downloaded on 12/28/2025 3:39:06 AM.
This article is licensed under a Creative Commons Attribution-NonCommercial 3.0 Unported Licence.

1. Introduction

Due to widespread concern over the shortage of fossil fuels, renewable and clean energy sources such as wind, solar, tidal and hydrogen have been developing rapidly in recent years.[1–3] Among them, green hydrogen energy has a high energy calorific value, wide source and high conversion efficiency, and can be used as an efficient energy storage carrier, which is considered as one of the most promising renewable clean energy sources.[4–6] Therefore, the production, transportation and storage of hydrogen are currently important research directions and urgent needs.[7,8] Compared with hydrogen production methods such as photocatalysis, electrocatalysis and biotransformation, catalytic reforming is the most likely way to achieve large-scale application.[9–11] At present, there are many reforming hydrogen production technologies for methane, formaldehyde, methanol, formic acid, ethanol and other small molecules.[12–14] Among them, methanol steam reforming has become one of the mainstream technologies for hydrogen production due to its mature technology, high methanol conversion rate and low CO content.[15] Although noble metal catalysts have excellent reforming hydrogen production performance and carbon deposition resistance, the cost is high, which is not conducive to large-scale application.[16–18] Therefore, the study of non-noble metal reforming catalysts for hydrogen production is of great significance.

NiO has excellent breaking ability of C–C, C–H and C–O bond and dehydrogenation ability, so it is often used as active component of reforming catalyst.[19–21] Titanium dioxide has become a commonly used catalyst carrier because of its excellent stability and mesoporous structure.[22–24] Meanwhile, NiO can produce a certain synergistic catalytic effect with TiO_2.[19] Therefore, theoretically NiO/TiO_2 catalyst can be used as one of the alternative catalysts for methanol reforming to produce hydrogen.[25] Furthermore, hierarchical porous structure is conducive to promoting the adsorption and activation of reaction molecules at the active sites on the catalyst surface, thereby improving the reaction activity.[26–28] Therefore, NiO loaded on TiO_2 surface and forming hierarchical porous structure should be able to make the catalyst have excellent methanol reforming activity.

Under the guidance of the above theory, Ni–Ti–O_x catalysts were prepared by using polyethylene oxide–polypropylene oxide–polyethylene oxide triblock copolymer (denoted as P123) as template and tetrabutyl titanate as gel at room temperature. In addition, according to the literature, the presence of chloride ions may have a certain role in promoting the performance of reforming hydrogen production,[29–31] so nickel chloride and nickel nitrate were used as precursors of NiO in this work. Based on the obtained Ni–Ti–O_x, the catalytic performance of Ni–Ti–O_x for methanol reforming to hydrogen was investigated, and the

[a]*School of Environmental Science and Engineering, Nanjing Tech University, Nanjing 210009, PR China. E-mail: htxu@njtech.edu.cn*

[b]*College of Materials Science and Engineering, Nanjing Tech University, Nanjing 210009, PR China*

[c]*Key Laboratory of Energy Thermal Conversion and Control of Ministry of Education, School of Energy and Environment, Southeast University, Nanjing, 210096, PR China*

[d]*Nanjing Gekof Institute of Environmental Protection Technology & Equipment Co., Nanjing 210031, PR China*

† Electronic supplementary information (ESI) available. See DOI: https://doi.org/10.1039/d3ra02891g

‡ These authors contributed equally to this work.

© 2023 The Author(s). Published by the Royal Society of Chemistry

Open Access Article. Published on 31 May 2023. Downloaded on 12/28/2025 3:39:06 AM.
This article is licensed under a Creative Commons Attribution-NonCommercial 3.0 Unported Licence.

reaction mechanism of methanol reforming to hydrogen was obtained by *in situ* DRIFT study and VASP calculation.

2. Experimental

The details about characterization were provided in ESI.†

2.1 Catalyst preparation

Synthesis of TiO_2. The P123 surfactant (2 g) with an average molecular weight of 5800 g mol^{-1} and citric acid monohydrate (5 g) as complexing agent were added to the mixed solution of ethanol (35 mL) and methanol (15 mL), and stirred for 1 h to obtain uniform precursor solution. Then 13 mL tetrabutyl titanate was dissolved and transparent solution was stirred at 35 °C for 4 h, and then placed at room temperature for 2 days. The obtained mixture was dried in air at 50 °C for 24 h. The dried samples were then calcined in a muffle furnace at 600 °C for 2 h.

Synthesis of Ni–Ti–O_x. When tetrabutyl titanate was added, appropriate amount of nickel chloride hexahydrate was added into the mixed solution at the same time, and the other steps were the same as the synthesis process of TiO_2. The loadings of nickel oxide were 5%, 10%, 15% and 20%, respectively. According to the different amounts of nickel chloride, the catalysts were abbreviated as 5% Ni–Ti–O_x, 10% Ni–Ti–O_x, 15% Ni–Ti–O_x and 20% Ni–Ti–O_x, respectively.

Synthesis of 5% Ni–Ti–O_x–N. The other steps were consistent with the preparation method of Ni–Ti–O_x, except replacing nickel chloride hexahydrate with nickel nitrate hexahydrate.

2.2 Catalysis measurement and characterization

The schematic diagram of the catalytic reaction device was shown in Fig. S1.† The flow rate of nitrogen (carrier gas) was 90 mL min^{-1}, and the mass ratio of methanol to deionized water was 2.5 to 1. The furnace was in horizontal position. The particle size of the catalyst was 0.63–0.85 mm, and its dosage was 1 g. The catalyst was not pretreated before the catalytic reaction. The weight hourly space velocity (MHSV) of reaction was 20 000 mL (g $h)^{-1}$. The mixture of methanol and deionized liquid was vaporized in the preheating furnace through a peristaltic pump, and then the mixture gas entered the reaction furnace and reacted with the catalyst. Finally, the gas after the reaction was passed into the gas chromatography for testing. The models and test methods for gas chromatography were described in detail in the ESI file.† The abbreviation of H_2, CO, CO_2 and CH_4 selectivity were S_{H_2}, S_{CO}, S_{CO_2} and S_{CH_4}, and the methanol conversion was abbreviated as X_m.

$$S_{H_2} = \frac{mol_{H_2}}{3 \times mol_m} \times 100\% \quad (1)$$

$$S_{CO} = \frac{mol_{CO}}{mol_m} \times 100\% \quad (2)$$

$$S_{CO_2} = \frac{mol_{CO_2}}{mol_m} \times 100\% \quad (3)$$

$$S_{CH_4} = \frac{mol_{CH_4}}{mol_m} \times 100\% \quad (4)$$

$$X_m = \frac{mol_{m_{out}}}{mol_{m_{in}}} \times 100\% \quad (5)$$

3. Results and discussion

3.1 Physical structure and chemical properties

Fig. 1 showed the X-ray diffraction (XRD) patterns of TiO_2 and Ni–Ti–O_x catalysts. For pure TiO_2, the characteristic diffraction peaks

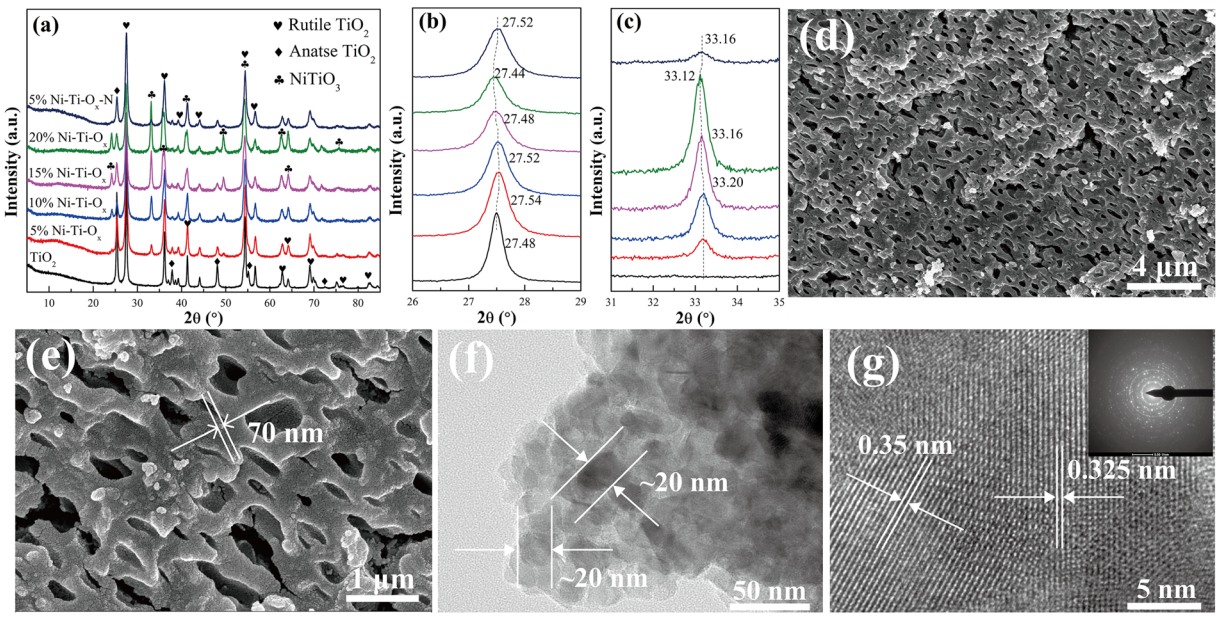

Fig. 1 (a) XRD patterns, (b) and (c) detail information of XRD patterns; (d) and (e) FE-SEM micrograph of 10% Ni–Ti–O_x catalyst; (f) and (g) HR-TEM micrograph of 10% Ni–Ti–O_x catalyst.

Open Access Article. Published on 31 May 2023. Downloaded on 12/28/2025 3:39:06 AM.
This article is licensed under a Creative Commons Attribution-NonCommercial 3.0 Unported Licence.

corresponded to rutile TiO_2 (PDF-ICDD 21-1276) and anatase TiO_2 (PDF-ICDD 21-1272), and the characteristic peak intensity of rutile TiO_2 was higher than that of anatase TiO_2. This indicated that TiO_2 was composed of two different crystal forms, and rutile was the main component. In addition, the characteristic diffraction peak corresponding to $NiTiO_3$ (PDF-ICDD 33-0960) appeared when NiO was doped with TiO_2. With the gradual increase of NiO content, the intensity of characteristic diffraction peak of TiO_2 gradually decreased, while that of $NiTiO_3$ gradually increased. It indicated that NiO did not exist on the surface of TiO_2 carrier in the form of nanoparticles, but reacted with some TiO_2 to form $NiTiO_3$ and was uniformly loaded on TiO_2. Meanwhile, the characteristic diffraction peaks of $NiTiO_3$ and TiO_2 gradually migrated to the low angle direction with the increase of NiO content (Fig. 1(b) and (c)). This may be due to the lattice distortion of TiO_2 caused by the existence of $NiTiO_3$.[21]

Fig. 1(d) and (e) showed the field emission scanning electron microscopy (FE-SEM) of 10% Ni–Ti–O_x catalyst. It could be seen from the figure that the catalyst was agglomerated by about 70 nm nanoparticles to form a micron-sized structure. In addition, there were abundant sub-micron pores (with the size of 250–800 nm) in the micron block particles, and the pores were interconnected. Combined with BET results, it could be seen that the Ni–Ti–O_x catalyst has both mesopores of about 2–20 nm and submicron pores of about 250–800 nm. In other words, Ni–Ti–O_x catalyst had hierarchical porous structure.

Fig. 1(e), (f) and S2–S4† showed the high-resolution transmission electron microscopy (HR-TEM) images and element mapping images of TiO_2 and 10% Ni–Ti–O_x catalysts, respectively. According to the Fig. S2 and S3,† the TiO_2 catalyst was composed of nanoparticles about 28–45 nm, and its lattice fringe spacing was 0.325 nm, corresponding to the (110) crystal plane of rutile TiO_2.[32–34] In addition, its element composition was also Ti and O elements, no other impurities appear. Corresponding to the results of TiO_2, the particle size of 10% Ni–Ti–O_x catalyst was about 20 nm, which indicated that the grain growth of TiO_2 was inhibited due to the formation of $NiTiO_3$. Combined with SEM and TEM data, it could be found that for the 10% Ni–Ti–O_x catalyst, the nanoparticles at about 20 nm were firstly agglomerated into submicron bulk particles at 70–150 nm, and then submicron particles were agglomerated to form micron particles with hierarchical pore structure. Furthermore, the lattice fringe spacing of 10% Ni–Ti–O_x catalyst were 0.35 nm and 0.325 nm, corresponding to (101) crystal plane of anatase TiO_2 and (110) crystal plane of rutile TiO_2, respectively.[35,36] Finally, according to the Fig. S4,† it could be found that Ni element was uniformly distributed in TiO_2. Combined with XRD data, it was proved that $NiTiO_3$ structure was formed in 10% Ni–Ti–O_x catalyst.

Fig. S5† and Table 1 showed the nitrogen adsorption and desorption curves, pore size distribution and specific surface area of TiO_2 and Ni–Ti–O_x catalysts. It could be seen that the nitrogen adsorption and desorption curves of all the six groups of catalysts have hysteresis loops, indicating that there were mesopores in the catalysts.[37] Furthermore, it could be seen from the pore size distribution that after a small amount of NiO was doped, the most probable pore size of the catalyst was 3.8 nm, and its average pore size was also reduced. On the contrary, when the NiO content was increased, the average pore diameter and the most probable pore diameter were increased. However, the 5% Ni–Ti–O_x catalyst had 30 $m^2\ g^{-1}$ and the others had close values to the 5% Ni–Ti–O_x.

3.2 Chemical properties

According to our previous studies, the hydroxyl group on the surface of metal oxide was one of the important reaction intermediates in the reforming reaction,[38] so the influence of acidity and alkalinity on the catalytic performance was extremely important. For Ni–Ti–O_x catalyst, TiO_2 was the main component, and the coordination charge number of oxygen was −2/3. One Ni atom in NiO was coordinated with six O atom, so the net charge value on each Ni–O bond was 1/3 − 2/3 = −1/3. According to Tanabe rule, the surface of NiO doped with TiO_2 was Brønsted acid.[39] In other words, the incorporation of NiO would increase the surface acidity of Ni–Ti–O_x catalyst. It could be seen from Fig. 2(a) that there were two ammonia desorption peaks of pure TiO_2 at 87 °C and 309 °C, representing physical adsorption and weak acidity, respectively.[40–42] With the increase of NiO content, the total acid quantity on the catalyst surface showed a trend of increasing first and then decreasing (Fig. 2(b)). It indicated that the incorporation of NiO could indeed significantly improve the acid quantity on the catalyst surface. Finally, by comparing the two groups of catalysts of 5% Ni–Ti–O_x and 5% Ni–Ti–O_x–N, it could be found that nickel chloride as a precursor had higher acid quantity than nickel nitrate as a precursor, and its acid strength was also significantly reduced, which was conducive to the improvement of catalytic activity of steam reforming for hydrogen production.

NiO is a basic oxide, so the incorporation of NiO can also theoretically enhance the basic surface of the catalyst. It could be seen from Fig. 2(c) that TiO_2 had two CO_2 desorption peaks at 100 °C and 299 °C, representing the weak basic site and the

Table 1 Physical properties of different catalysts

Samples	BET surface area/($m^2\ g^{-1}$)	Pore volume/($cm^3\ g^{-1}$)	Average pore diameter/nm	Most probable pore size/nm
TiO_2	26.0	0.0816	17.7	9.7
5% Ni–Ti–O_x	30.0	0.0649	13.2	3.8
10% Ni–Ti–O_x	32.7	0.0778	14.7	7.9
15% Ni–Ti–O_x	39.9	0.1240	16.1	12.6
20% Ni–Ti–O_x	31.3	0.1187	18.3	12.7
5% Ni–Ti–O_x–N	29.6	0.0694	9.5	3.8

© 2023 The Author(s). Published by the Royal Society of Chemistry

Open Access Article. Published on 31 May 2023. Downloaded on 12/28/2025 3:39:06 AM.
This article is licensed under a Creative Commons Attribution-NonCommercial 3.0 Unported Licence.

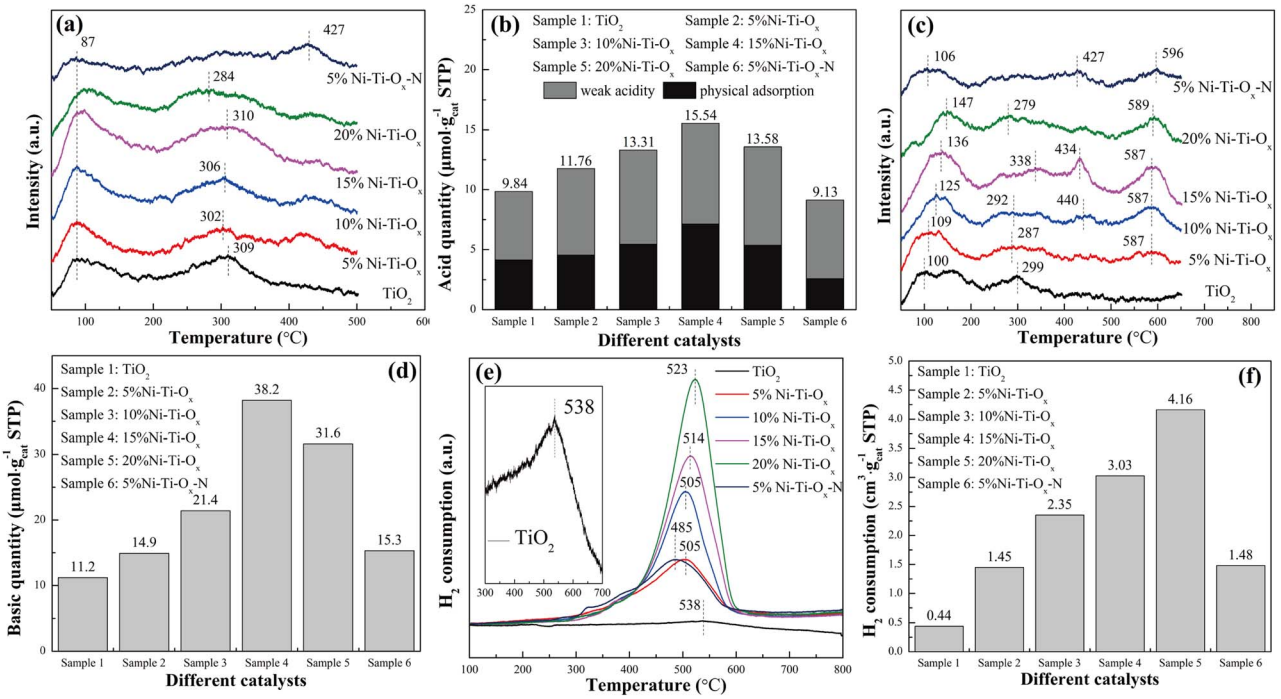

Fig. 2 (a) NH_3-TPD profiles, (b) acid quantity, (c) CO_2-TPD profiles, (d) basic quantity, (e) H_2-TPR profiles, (f) H_2 consumption of different catalysts.

medium basic site, respectively.[43,44] When NiO was doped, two obvious CO_2 desorption peaks appeared near 440 °C and 590 °C, corresponding to the strong basic site, which may be attributed to the role of $NiTiO_3$. In addition, with the gradual increase of NiO content, the basic quantity on the catalyst surface increased from 11.2 μmol $g_{cat.}^{-1}$ of TiO_2 to 38.2 μmol $g_{cat.}^{-1}$ of 15% Ni–Ti–O_x. However, as the content of NiO continued to increase, the basic quantity on the catalyst surface began to decrease (Fig. 2(d)). It may be because the content of NiO was too high, so that the active site was gradually covered by coating. Finally, according to our previous research, carboxylic acid species may appear in the intermediate species of methanol reforming to hydrogen production, so the enhancement of catalyst surface basic may be beneficial to the improvement of catalytic activity.

Redox performance was one of the important factors affecting the hydrogen production performance of reforming, so six groups of catalysts were characterized by H_2-TPR, and the results were shown in Fig. 2(e) and (f). It was seen that pure TiO_2 had a hydrogen reduction peak at 538 °C, corresponding to the reduction of Ti^{4+}–O–Ti^{4+}.[45–47] The reduction peak of Ni–Ti–O_x migrated to low temperature after the addition of NiO and the hydrogen consumption of the catalyst increased linearly with the increase of NiO content (Fig. S6†). Therefore, the hydrogen reduction peak at 485–523 °C should correspond to the reduction of Ni^{2+}–O–Ti^{4+}. This indicated that $NiTiO_3$ exhibited better redox performance than TiO_2. The increase of hydrogen consumption also indicated that the catalyst surface had more hydroxyl groups, which was beneficial to the catalytic reaction. Finally, with the increase of NiO content, the hydrogen consumption of the catalyst increased, but the hydrogen reduction peak temperature also gradually increased. That was to say, the number of hydroxyl groups that could easily participate in the reaction was also gradually decreasing. Therefore, Ni–Ti–O_x catalyst had an optimal equilibrium point between redox performance and hydrogen consumption to achieve the best catalytic performance.

3.3 Surface active species

Fig. 3 and Table 2 showed the XPS results of TiO_2 and Ni–Ti–O_x catalysts. As shown in Fig. 3(a), there were not only peaks of O 1s and Ti 2p, but also peaks of Na in all samples, which may be due to impurities in tetrabutyl titanate or P123. In addition, the peak intensity of Ni 2p gradually increased with the increase of NiO content. According to Fig. 3(b), O 1s could be divided into two peaks of 531 eV and 529.5 eV, corresponding to chemisorbed oxygen (O_α) and the lattice oxygen (O_β), respectively.[48,49] According to the literature, chemisorbed oxygen was the most active oxygen in the catalytic reaction, so the increase of its concentration was conducive to the catalytic reaction.[48,50] It could be found that the proportion of chemisorbed oxygen on the catalyst surface increased from 0.154 to 0.214 with the increase of NiO content. In other words, the incorporation of NiO could effectively promoted the increase of chemisorbed oxygen concentration, thus accelerating the reaction. This was consistent with the hydrogen consumption in H_2-TPR results.

Fig. 3(c) showed Ti 2p peaks of TiO_2 and Ni–Ti–O_x catalysts. It could be seen that the Ti 2p peak of pure TiO_2 was divided into three peaks at 464.4 eV, 463.5 eV and 458.5 eV, corresponding to Ti^{4+} and Ti^{3+}.[51] When NiO was doped, the Ti 2p peaks of all catalysts migrated to the low electron binding

Open Access Article. Published on 31 May 2023. Downloaded on 12/28/2025 3:39:06 AM.
This article is licensed under a Creative Commons Attribution-NonCommercial 3.0 Unported Licence.

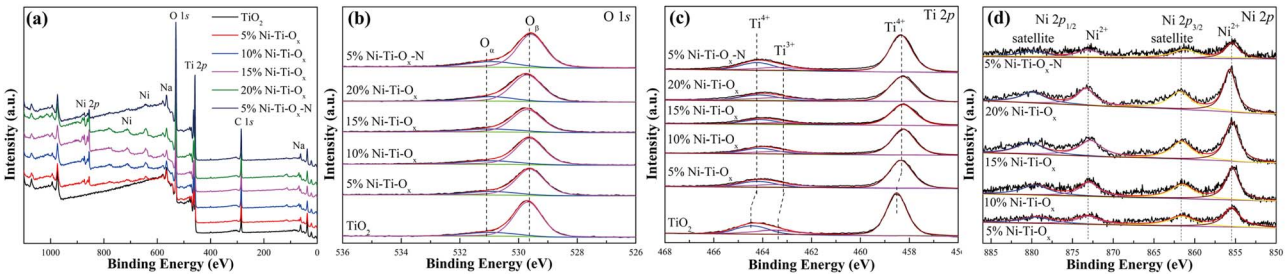

Fig. 3 (a) Survey, (b) O 1s, (c) Ti 2p and (d) Ni 2p XPS high-resolution scans spectra of different catalysts.

Table 2 Atomic distribution of different catalysts

Sample	$Ti^{3+}/(Ti^{3+} + Ti^{4+})$	$O_\alpha/(O_\alpha + O_\beta)$
TiO_2	0.193	0.154
5% Ni–Ti–O_x	0.181	0.175
10% Ni–Ti–O_x	0.177	0.192
15% Ni–Ti–O_x	0.175	0.204
20% Ni–Ti–O_x	0.192	0.214
5% Ni–Ti–O_x–N	0.185	0.198

energies. It indicated that the formation of $NiTiO_3$ changed the chemical environment around TiO_2. In addition, the decrease of Ti 2p peak intensity after NiO doping was mainly due to the decrease of the relative content of TiO_2 in the catalyst. Finally, it was seen from Table 2 that the concentration of Ti^{3+} ions gradually decreased with the incorporation of NiO. This may be due to the reaction of some Ti^{3+} ions with NiO to form $NiTiO_3$, which converted to Ti^{4+} ions. Fig. 3(d) showed the Ni 2p spectra of TiO_2 and Ni–Ti–O_x catalysts. Ni 2p was divided into satellite (879.5 eV and 861.5 eV) and Ni^{2+} (872.9 eV and 855.4 eV).[52] Furthermore, the intensity of Ni 2p peak gradually increased due to the gradual increase of NiO content in the catalyst. Finally, only one valence state of Ni^{2+} was found in the catalysts. Combined with XRD and other data, $NiTiO_3$ was indeed formed in the catalysts.

3.4 Catalytic performance

Fig. 4 and S7† showed the selectivity and conversion of TiO_2 and Ni–Ti–O_x catalysts. It was seen from Fig. 4(a) that pure TiO_2 reached the hydrogen selectivity of only 8.6% at 450 °C. This was mainly because pure TiO_2 had the lowest redox performance, hydrogen consumption, surface acid quantity and surface basic quantity among the six groups of catalysts, and TiO_2 did not have the same C–O and C–C bond breaking ability as NiO. With the gradual increase of NiO content, the hydrogen selectivity of Ni–Ti–O_x catalyst showed a parabolic trend of first increase and then decrease. Meanwhile, 10% Ni–Ti–O_x catalyst had the highest hydrogen selectivity, and its hydrogen selectivity was higher than 90% in the range of 550–600 °C. The T_{50} temperature (the temperature at which the hydrogen selectivity reached 50%) was also the lowest, which was 450 °C. Combined with the above characterization results, it could be seen that the redox performance and hydrogen consumption were the two most important parameters for the hydrogen production performance of methanol steam reforming. Finally, comparing the hydrogen selectivity of 5% Ni–Ti–O_x and 5% Ni–Ti–O_x–N catalysts, it was found that 5% Ni–Ti–O_x catalyst had lower acid strength and alkali strength, so its hydrogen selectivity was higher. This indicated that the acidity and alkalinity of the catalyst surface were also important parameters affecting the performance of methanol steam reforming for hydrogen production.

Fig. 4(b) and (c) showed CO selectivity and CO_2 selectivity of TiO_2 and Ni–Ti–O_x catalysts, respectively. Similar to the results of hydrogen selectivity, 10% Ni–Ti–O_x catalyst had the highest CO selectivity (92.6%) at 500 °C, while the highest CO selectivity of pure TiO_2 was only 16.1% at 450 °C. In addition, the CO selectivity of the six groups of catalysts reached the highest at about 450 °C or 500 °C, and then decreased with the increase of temperature. Correspondingly, except that the CO_2 selectivity of TiO_2 was always lower than 1.1%, that of the other five groups of Ni–Ti–O_x catalysts increased slowly with the increase of temperature before 450 °C or 500 °C, but increased sharply in the temperature range of 450–600 °C or 500–600 °C. It was speculated that the methanol steam reforming reaction was dominated by $CH_3OH \rightarrow H_2 + CO$ below 500 °C and $CH_3OH + H_2O \rightarrow H_2 + CO$ at 500–600 °C.

Fig. S7† showed the CH_4 selectivity of TiO_2 and Ni–Ti–O_x catalysts. It was found that CH_4 selectivity of TiO_2 and 20% Ni–Ti–O_x catalysts was relatively high, reaching 32.2% at 450 °C and 37.7% at 500 °C, respectively. Correspondingly, the CH_4 selectivity of the optimal catalyst 10% Ni–Ti–O_x was lower than 12.1% in the whole test temperature range of 350–600 °C. Combined with the results of H_2, CO and CO_2 selectivity, it was speculated that there were many side reactions for pure TiO_2 or Ni–Ti–O_x catalysts with excessive NiO doping. Accordingly, the optimal catalyst 10% Ni–Ti–O_x had less side reaction. Finally, it was seen from Fig. 4(d) that the methanol conversion of 10% Ni–Ti–O_x catalyst reached 88.4% at 400 °C, and that was higher than 92% at 450–600 °C. As shown in Table 3, the catalytic performance of 10% Ni–Ti–O_x was compared with that of other catalysts from the literature. It was verified that NiO/MoO_3 had some degree of advantages from the aspects of initiation temperature (the temperature at which the H_2 selectivity was higher than 50%), highest hydrogen selectivity. However, the initiation temperature was relatively high and needed to be optimized for subsequent experiments.

© 2023 The Author(s). Published by the Royal Society of Chemistry

Open Access Article. Published on 31 May 2023. Downloaded on 12/28/2025 3:39:06 AM.
This article is licensed under a Creative Commons Attribution-NonCommercial 3.0 Unported Licence.

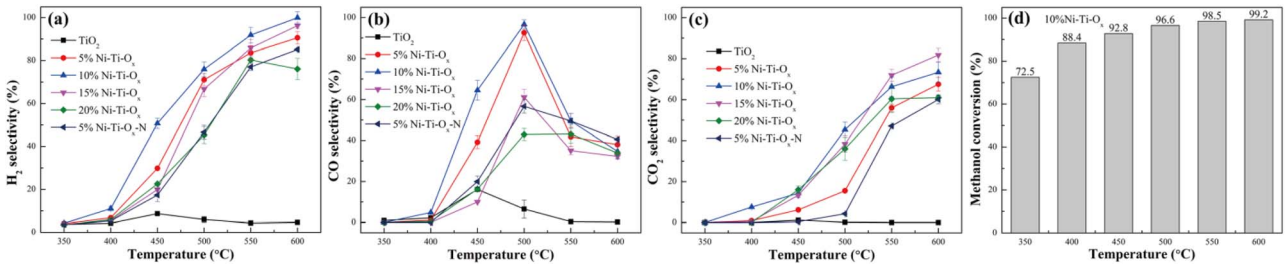

Fig. 4 (a) H_2 selectivity, (b) CO selectivity and (c) CO_2 selectivity of different catalysts; (d) methanol conversion of 10% Ni–Ti–O_x catalyst.

3.5 *In situ* DRIFTS study

Fig. 5 and S8† showed the *in situ* diffuse reflectance infrared spectra of methanol adsorption and methanol–H_2O reaction of pure TiO_2 at different temperatures. It was seen from Fig. 5(a) that with the extension of methanol adsorption time, the main peaks represented hydroxyl group (3670 cm^{-1}), methoxy species (CH_3O*, 2984, 2897 and 1057 cm^{-1}), gaseous formaldehyde (1760–1722 cm^{-1}), formic acid species ($HCOO_{ad}$, 1615 and 1387 cm^{-1}) and the ν(OH) of molecular-adsorbed ethanol (1238 cm^{-1}), respectively. The emergence of methoxy species, formaldehyde species and formic acid species indicated that the path of methanol reforming to hydrogen production was similar to that of our previous study.[14] In other words, methanol was adsorbed on the surface of the catalyst to form adsorbed methanol, and then dehydrogenation to form formaldehyde species. Formaldehyde species reacted with hydroxyl groups on the surface of the catalyst and adsorbed water molecules. Finally, hydrogen, carbon monoxide and carbon dioxide were generated. However, the presence of molecular-adsorbed ethanol indicated that the methoxy species of pure TiO_2 also reacted with adsorbed methanol during the reaction, resulting in by-products. This was also why the H_2 selectivity and CO_2 selectivity of pure TiO_2 were low, but the CO selectivity and CH_4 selectivity were high.

As shown in Fig. 5(b) and (c), after the adsorption of methanol for 10 min, the *in situ* infrared spectra did not change significantly whether the water vapor was introduced or both water vapor and methanol were introduced. Only the peak intensity representing methoxy species was slightly enhanced. This was mainly because the H_2 selectivity, CO selectivity, CO_2 selectivity and CH_4 selectivity were at a very low level at 400 °C. The peaks of all intermediate species decreased significantly

Table 3 The comparison with the catalytic performance of reported catalysts

Catalyst	Initiation temperature (°C)	Highest H_2 selectivity (%)	Ref.
10% Ni–Ti–O_x	450	99.9	This work
8Ni/TCW	400	99.4	37
Cu/ZnO/Al_2O_3	—	89.0	53
10La–10Ni/Al_2O_3	200	85.0	54
Cu–Ni/TiO_2/monolith	300	85.8	55
TiO_2–P25	400	40.0	56
TiO_2–X	400	70.0	57
Pd/TiO_2	250	65.0	58

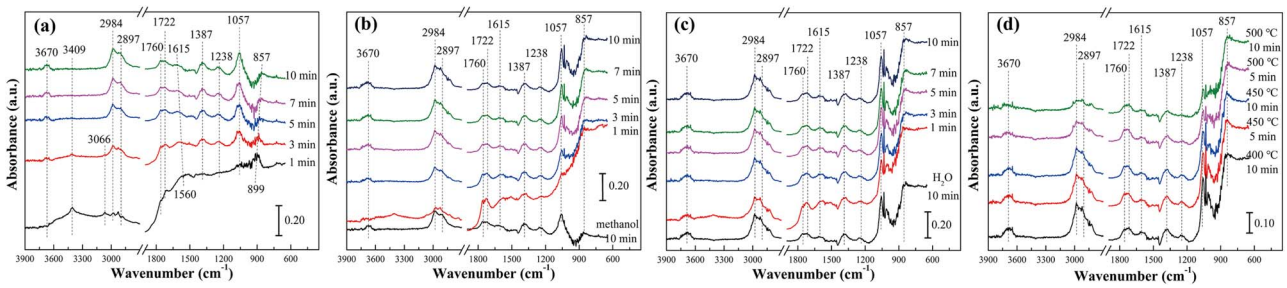

Fig. 5 *In situ* DRIFT spectra of TiO_2 catalyst at different temperatures: (a) methanol adsorption at 400 °C, (b) H_2O adsorption at 400 °C, (c) methanol reacted with H_2O at 400 °C and (d) methanol reacted with H_2O at different temperatures.

Open Access Article. Published on 31 May 2023. Downloaded on 12/28/2025 3:39:06 AM.
This article is licensed under a Creative Commons Attribution-NonCommercial 3.0 Unported Licence.

Table 4 Details of the bands and corresponding species

Band (cm^{-1})	Species	Ref.
3715–3670	Hydroxyl group	59
2984–2820, 1057	Methoxy species (CH_3O*)	60
1760–1722	Gaseous formaldehyde	61
1703	ν(CO) in $HCOOH_{ad}$	62
1615–1353	ν_{as}(COO) in $HCOO_{ad}$	63
1238	The ν(OH) of molecular-adsorbed ethanol	64

when the reaction temperature increased to 450 °C and 500 °C (Fig. 5(d) and S8†). It indicated that methoxy species, formaldehyde, formic acid species and molecular-adsorbed ethanol were involved in the reaction. According to the peak intensity and its variation, it was speculated that methoxy species and formic acid species were the main intermediate species of methanol steam reforming reaction over the TiO_2 catalyst. Meanwhile, the hydroxyl group on the catalyst surface was gradually consumed again, indicating that the hydroxyl group was also an important intermediate of the reaction (Table 4).

In order to compare the reaction mechanism of pure TiO_2 and Ni–Ti–O_x catalysts, 10% Ni–Ti–O_x catalyst was selected for *in situ* infrared characterization. The results were shown in Fig. 6 and S9.† According to Fig. 6(a), after methanol adsorption for 10 min, methoxy species (2919 and 2820 cm^{-1}), formic acid species (1580 and 1467 cm^{-1}), and formic acid adsorption species ($HCOOH_{ad}$, 1703 cm^{-1}) that formed hydrogen bonds with hydroxyl groups on the surface of 10% Ni–Ti–O_x catalyst appeared. Compared with the results of pure TiO_2, gaseous formaldehyde and molecular-adsorbed ethanol did not appear in the spectrum of 10% Ni–Ti–O_x catalyst, which was mainly because 10% Ni–Ti–O_x had better redox performance and higher selectivity.

Similar to the results of pure TiO_2, the spectrum of 10% Ni–Ti–O_x did not change significantly after methanol was added for 10 min and water vapor was added (Fig. 6(b)). When water vapor and methanol were simultaneously introduced, the peak intensity of hydroxyl group, methoxy species and formic acid species gradually decreased with time (Fig. 6(c)). It could be speculated that these three intermediates were involved in the steam reforming reaction for hydrogen production. From Fig. 6(d) and S9,† the peak intensity of hydroxyl group, methoxy species and formic acid species gradually continued to decrease. Based on the results of *in situ* infrared diffuse reflection characterization and catalytic activity, it could be found that there were two main reaction pathways for methanol steam reforming on the surface of 10% Ni–Ti–O_x catalyst (Fig. 7): (1)

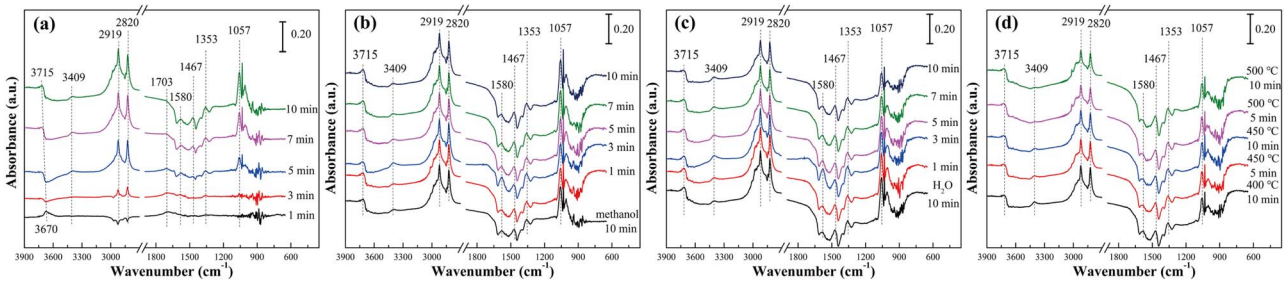

Fig. 6 *In situ* DRIFT spectra of 10% Ni–Ti–O_x catalyst at different temperatures: (a) methanol adsorption at 400 °C, (b) H_2O adsorption at 400 °C, (c) methanol reacted with H_2O at 400 °C and (d) methanol reacted with H_2O at different temperatures.

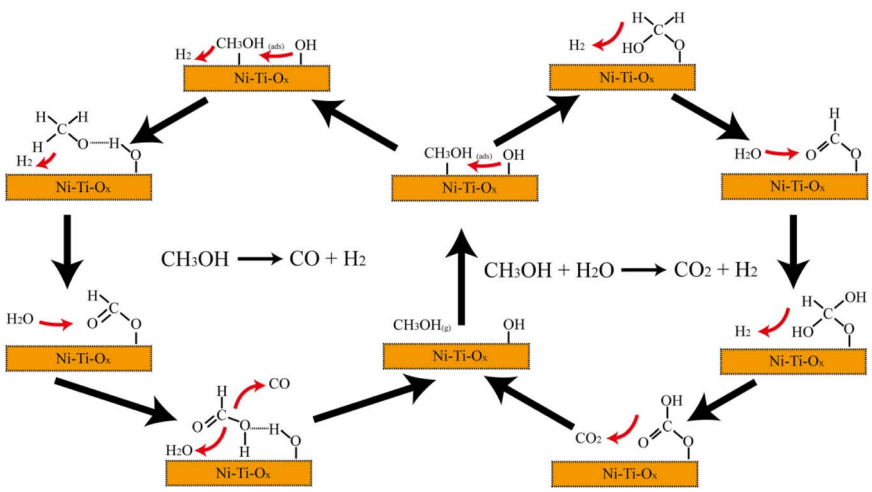

Fig. 7 Reaction mechanism diagram of Ni–Ti–O_x catalyst.

© 2023 The Author(s). Published by the Royal Society of Chemistry

Open Access Article. Published on 31 May 2023. Downloaded on 12/28/2025 3:39:06 AM. This article is licensed under a Creative Commons Attribution-NonCommercial 3.0 Unported Licence.

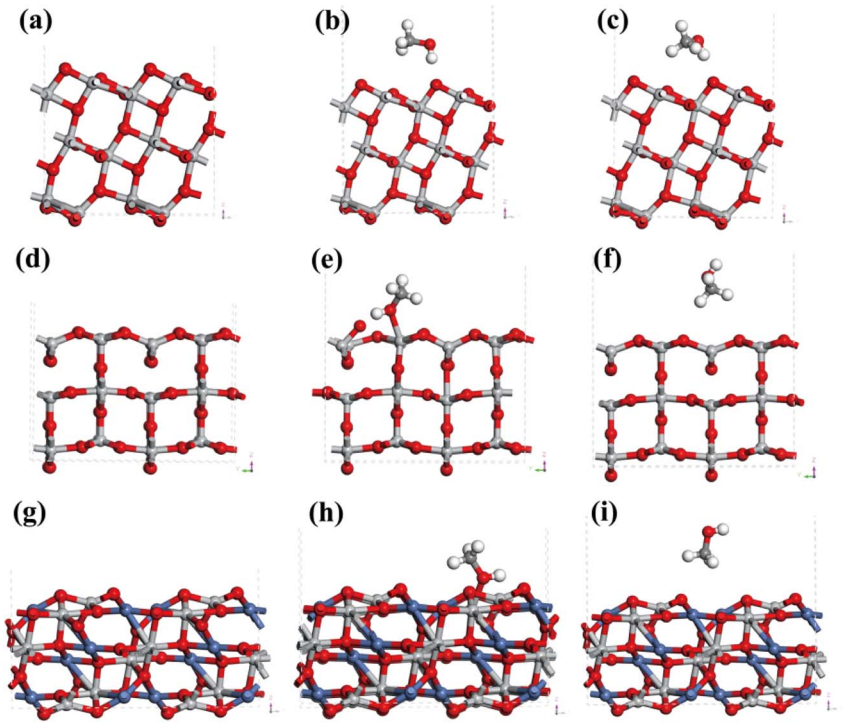

Fig. 8 (a) The (101) facet of anatase TiO_2, (b) the first CH_3OH adsorption model (site 1) on the (101) facet of anatase TiO_2, (c) the second CH_3OH adsorption model (site 2) on the (101) facet of anatase TiO_2; (d) the (110) facet of rutile TiO_2, (e) the first CH_3OH adsorption model (site 1) on the (110) facet of rutile TiO_2, (f) the second CH_3OH adsorption model (site 2) on the (110) facet of rutile TiO_2; (g) the (104) facet of $NiTiO_3$, (h) the first CH_3OH adsorption model (site 1) on the (104) facet of $NiTiO_3$, (i) the second CH_3OH adsorption model (site 2) on the (104) facet of $NiTiO_3$.

Table 5 The adsorption energy of CH_3OH on different catalysts

	Site 1	Site 2
Sample	Adsorption energy (eV)	Adsorption energy (eV)
Anatase TiO_2	−0.165	−0.229
Rutile TiO_2	−0.681	−0.230
$NiTiO_3$	−1.106	−0.038

methanol was decomposed into methoxy intermediates and hydrogen was generated, and then methoxy continued to decompose; (2) methanol was oxidized to formic acid species, and then reacted with the surface hydroxyl group of the catalyst to generate CO_2 and hydrogen, in which water vapor mainly supplemented the surface hydroxyl of the catalyst. Therefore, it was speculated that the methanol steam reforming reaction followed both L–H and E–R mechanisms.

3.6 Adsorption energy calculation

This work simulated the adsorption behaviors that CH_3OH on the surface of anatase TiO_2, rutile TiO_2 and $NiTiO_3$ using the tool of Vienna *Ab initio* Simulation Package (VASP). According to XRD and TEM results, TiO_2 in Ni–Ti–O_x catalyst could be divided into anatase TiO_2 and rutile TiO_2, and the main exposed crystal planes of anatase TiO_2 and rutile TiO_2 were (101) and (110), respectively. From Fig. 8(a)–(c) and S10(a)–(c),† the (101) crystal plane of anatase TiO_2 was cut and optimized. In order to compare the effect of the position of the methanol molecule on the adsorption energy, two methanol adsorption models (site 1 and site 2) were simulated. Correspondingly, two adsorption models of methanol molecules on the (110) crystal plane of rutile TiO_2 were optimized (Fig. 8(d)–(f) and S10(d)–(f)†). Comparing the adsorption energy of methanol molecules of the two TiO_2 (Table 5), it could be found that rutile TiO_2 may be easier to adsorb methanol molecules. That was to say, the presence of rutile TiO_2 in the Ni–Ti–O_x catalyst was beneficial to the adsorption and activation of methanol molecules.

The active component NiO in the Ni–Ti–O_x catalyst mainly existed in the form of $NiTiO_3$, and its main exposed crystal plane was (104). Therefore, Fig. 8(h), (i), S10(h) and (i)† mainly showed two adsorption models of methanol molecules on its (104) crystal face. It was found that the adsorption energy of $NiTiO_3$ for methanol molecules was significantly higher than that of TiO_2. Combined with the results of H_2-TPR, CO_2-TPD and XPS, it could be found that the formation of $NiTiO_3$ was more conducive to the adsorption and activation of methanol molecules. This was one of the reasons why the Ni–Ti–O_x catalyst exhibited excellent methanol steam reforming hydrogen production performance.

4. Conclusions

In this work, Ni–Ti–O_x nanocatalysts with hierarchical porous structure were prepared and the catalytic performance for

Open Access Article. Published on 31 May 2023. Downloaded on 12/28/2025 3:39:06 AM. This article is licensed under a Creative Commons Attribution-NonCommercial 3.0 Unported Licence.

methanol steam reforming was investigated. It was found that NiO in the Ni–Ti–O_x catalyst existed in the form of $NiTiO_3$, and both anatase TiO_2 and rutile TiO_2 existed in the carrier. Therefore, it exhibited excellent redox properties, high concentration of chemisorbed oxygen, rich basic sites and acidic sites. The optimal catalyst 10%Ni–Ti–O_x had H_2 selectivity higher than 90% and methanol conversion higher than 95% at 550–600 °C. Furthermore, the reaction path of methanol steam reforming of Ni–Ti–O_x was studied by *in situ* infrared diffuse reflectance spectroscopy. Hydroxyl group, methoxy species and formic acid species were the main intermediates. Finally, the formation of $NiTiO_3$ enhanced the adsorption energy of methanol molecules on the surface of Ni–Ti–O_x catalyst, which promoted the adsorption and activation of methanol molecules.

Author contributions

Qijie Jin: data curation, formal analysis, roles/writing-original draft, funding acquisition. Xuelu Meng: roles/writing-original draft, formal analysis. Peng Wu: computer simulation. Yunhe Li: data curation, formal analysis. Mutao Xu: data curation, formal analysis. Ranran Zhou: methodology, investigation. Mengfei Yang: methodology, formal analysis. Haitao Xu: supervision, validation, funding acquisition, project administration.

Conflicts of interest

There are no conflicts to declare.

Acknowledgements

We would like to acknowledge the financial support from the Natural Science Foundation of Jiangsu Province (BK20220365), National Key Research and Development Program of China (2021YFB3500600, 2021YFB3500605), Industry-University-Research Cooperation Project of Jiangsu Province (BY2022514), Natural Science Foundation of the Jiangsu Higher Education Institutions of China (22KJB610002), Key R&D Program of Jiangsu Province (BE2022142), Jiangsu International Cooperation Project (BZ2021018), Jiangsu Funding Program for Excellent Postdoctoral Talent (2022ZB375), Science and Technology Plan of Yangzhou (YZ2022030), Nanjing Science and Technology Top Experts Gathering Plan and the Priority Academic Program Development of Jiangsu Higher Education Institutions (PAPD). The computational resources generously provided by the High Performance Computing Center of Nanjing Tech University were greatly appreciated. Qijie Jin also thanks Hong Zhou from the School of Materials Science and Engineering, Nanjing Tech University, for helping to characterize the catalyst activity.

Notes and references

1 M. G. Schultz, T. Diehl, G. P. Brasseur and W. Zittel, *Science*, 2003, **302**, 624–627.
2 V. G. Sharmila, K. Tamilarasan, M. D. Kumar, G. Kumar, S. Varjani, S. A. Kumar and J. R. Banu, *Int. J. Hydrog. Energy*, 2022, **47**, 15309–15332.
3 A. Kumar, P. Daw and D. Milstein, *Chem. Rev.*, 2022, **122**, 385–441.
4 H. Wang, L. Wang, D. Lin, X. Feng, X. F. Chu, L. N. Li and F. S. Xiao, *Catal. Today*, 2021, **382**, 42–47.
5 H. Y. Lian, J. L. Liu, X. S. Li, X. B. Zhu, A. Z. Weber and A. M. Zhu, *Chem. Eng. J.*, 2019, **369**, 245–252.
6 Y. C. Wang, Q. Wu, D. Q. Mei and Y. D. Wang, *Int. J. Hydrog. Energy*, 2020, **45**, 25317–25327.
7 A. C. Avci and E. Toklu, *Int. J. Hydrog. Energy*, 2022, **47**, 6986–6995.
8 M. Q. Chen, G. W. Sun, Y. S. Wang, D. F. Liang, C. Li, J. Wang and Q. Liu, *Fuel*, 2022, **314**, 122733.
9 Y. Q. Xu, B. W. Lu, C. Luo, J. Chen, Z. W. Zhang and L. Q. Zhang, *Chem. Eng. J.*, 2021, **406**, 126903.
10 I. V. Yentekakis, P. Panagiotopoulou and G. Artemakis, *Appl. Catal., B*, 2021, **296**, 120210.
11 M. Bianchini, N. Alayo, L. Soler, M. Salleras, L. Fonseca, J. Llorca and A. Tarancon, *J. Power Sources*, 2021, **506**, 230241.
12 A. Al-Qahtani, B. Parkinson, K. Hellgardt, N. Shah and G. Guillen-Gosalbez, *Appl. Energy*, 2021, **281**, 115958.
13 K. H. Han, W. S. Yu, L. L. Xu, Z. Y. Deng, H. Yu and F. G. Wang, *Fuel*, 2021, **291**, 120182.
14 Q. J. Jin, Y. S. Shen, Y. Cai, L. Chu and Y. W. Zeng, *J. Hazard. Mater.*, 2020, **381**, 120934.
15 L. L. Lin, W. Zhou, R. Gao, S. Y. Yao, X. Zhang, W. Q. Xu, S. J. Zheng, Z. Jiang, Q. L. Yu, Y. W. Li, C. Shi, X. D. Wen and D. Ma, *Nature*, 2017, **544**, 80.
16 S. Alayoglu, A. U. Nilekar, M. Mavrikakis and B. Eichhorn, *Nat. Mater.*, 2008, **7**, 333–338.
17 K. Ghasemzadeh, E. Andalib and A. Basile, *Int. J. Hydrog. Energy*, 2016, **41**, 8745–8754.
18 J. Saavedra, T. Whittaker, Z. Chen, C. J. Pursell, R. M. Rioux and B. D. Chandler, *Nat. Chem.*, 2016, **8**, 585–590.
19 T. Abbas and M. Tahir, *Int. J. Hydrog. Energy*, 2021, **46**, 8932–8949.
20 C. Wu, Z. R. Xiao, L. Wang, G. Z. Li, X. W. Zhang and L. C. Wang, *Catal. Sci. Technol.*, 2021, **11**, 1965–1973.
21 S. S. Zhu, Y. Z. Wang, J. C. Lu, H. H. Lu, S. F. He, D. Song, Y. M. Luo and J. P. Liu, *Nanomaterials*, 2021, **11**, 3149.
22 X. L. Liu, C. Bao, Z. H. Zhu, H. B. Zheng, C. Song and Q. Xu, *Int. J. Hydrog. Energy*, 2021, **46**, 26741–26756.
23 K. Gao, O. A. Sahraei and M. C. Iliuta, *Appl. Catal., B*, 2021, **291**, 119958.
24 K. S. Baamran and M. Tahir, *J. Clean. Prod.*, 2021, **311**, 127519.
25 T. T. Xu, C. Jiang, X. Wang and B. Xiao, *Energy Convers. Manage.*, 2021, **244**, 114512.
26 J. Xiong, X. L. Mei, J. Liu, Y. C. Wei, Z. Zhao, Z. A. Xie and J. M. Li, *Appl. Catal., B*, 2019, **251**, 247–260.
27 X. L. Wang, P. Du, Z. Zhao, J. L. Mei, Z. T. Chen, Y. Y. Li, P. Zheng, J. Y. Fan, A. J. Duan and C. M. Xu, *Energy Fuels*, 2018, **32**, 7800–7809.

© 2023 The Author(s). Published by the Royal Society of Chemistry

Open Access Article. Published on 31 May 2023. Downloaded on 12/28/2025 3:39:06 AM. This article is licensed under a Creative Commons Attribution-NonCommercial 3.0 Unported Licence.

28 T. Wang, L. Chang, H. Wu, W. H. Yang, J. R. Cao, H. Fan, J. Q. Wang, H. T. Liu, Y. H. Hou, Y. C. Jiang and H. Zhu, *J. Colloid Interface Sci.*, 2022, **612**, 434–444.
29 Z. W. Xue, Y. S. Shen, L. Chu, Y. Wang, Y. Zhang, Z. F. Sun, J. H. Wang, Y. W. Zeng, P. W. Li and S. M. Zhu, *J. Mater. Chem. A*, 2019, **7**, 1700–1710.
30 Z. W. Xue, Y. S. Shen, P. W. Li, Y. Zhang, J. J. Li, B. Qin, J. Zhang, Y. W. Zeng and S. M. Zhu, *Small*, 2018, **14**, 1800927.
31 C. T. Zhang, X. L. Qin, Z. W. Xue, X. B. Wang, Y. S. Shen, J. W. Zhu, Y. N. Wu, B. Meng, X. X. Meng and N. T. Yang, *Chem. Eng. J.*, 2022, **433**, 134600.
32 Q. Guo, C. Y. Zhou, Z. B. Ma and X. M. Yang, *Adv. Mater.*, 2019, **31**, 1901997.
33 Y. G. Wang, Y. Yoon, V. A. Glezakou, J. Li and R. Rousseau, *J. Am. Chem. Soc.*, 2013, **135**, 10673–10683.
34 J. C. Liu, Y. G. Wang and J. Li, *J. Am. Chem. Soc.*, 2017, **139**, 6190–6199.
35 A. Wang, S. J. Wu, J. L. Dong, R. X. Wang, J. W. Wang, J. L. Zhang, S. X. Zhong and S. Bai, *Chem. Eng. J.*, 2021, **404**, 127145.
36 C. C. Ni, Y. F. Li, X. Z. Meng, S. L. Liu, S. Y. Luo, J. Guan and B. Jiang, *Chem. Eng. J.*, 2021, **411**, 128485.
37 Q. J. Jin, Y. S. Shen, L. Chu, M. M. Chen, Y. Cai and Y. W. Zeng, *Composites, Part B*, 2019, **178**, 107483.
38 Q. J. Jin, A. D. Wang, B. X. Lu, X. Xu, Y. S. Shen and Y. W. Zeng, *Catal. Sci. Technol.*, 2020, **10**, 4436–4447.
39 Q. J. Jin, M. M. Chen, X. J. Tao, B. X. Lu, J. Y. Shen, Y. S. Shen and Y. W. Zeng, *Appl. Surf. Sci.*, 2020, **512**, 145757.
40 L. Na, S. L. Ding, Y. M. Cui, N. H. Xue, L. M. Peng, X. F. Guo and W. P. Ding, *Chem. Eng. Res. Des.*, 2013, **91**, 573–580.
41 D. C. Baertsch, T. K. Komala, Y. H. Chua and E. Iglesia, *J. Catal.*, 2002, **205**, 44–57.
42 Y. S. Shen, Y. H. Zong, Y. F. Ma, S. M. Zhu and Q. J. Jin, *Fuel*, 2016, **180**, 727–736.
43 S. Tada, T. Shimizu, H. Kameyama, T. Haneda and R. Kikuchi, *Int. J. Hydrog. Energy*, 2012, **37**, 5527–5531.
44 A. S. Al-Fatesh, Y. Arafat, S. O. Kasim, A. A. Ibrahim, A. E. Abasaeed and A. H. Fakeeha, *Appl. Catal., B*, 2021, **280**, 119445.
45 H. F. Chen, Y. Xia, R. Y. Fang, H. Huang, Y. P. Gan, C. Liang, J. Zhang, W. K. Zhang and X. S. Liu, *Appl. Surf. Sci.*, 2018, **459**, 639–646.
46 S. Besselmann, C. Freitag, O. Hinrichsen and M. Muhler, *Phys. Chem. Chem. Phys.*, 2001, **3**, 4633–4638.
47 Z. L. Chen, Y. Jian, J. H. Yan, F. Dong and B. F. Yin, *Chem. Eng. Sci.*, 2022, **262**, 118006.
48 M. Kang, E. D. Park, J. M. Kim and J. E. Yie, *Appl. Catal., A*, 2007, **327**, 261–269.
49 Q. L. Zhang, X. Liu, P. Ning, Z. X. Song, H. Li and J. J. Gu, *Catal. Sci. Technol.*, 2015, **5**, 2260–2269.
50 Z. B. Wu, R. B. Jin, H. Q. Wang and Y. Liu, *Catal. Commun.*, 2009, **10**, 935–939.
51 Y. Liu, P. F. Fang, Y. L. Cheng, Y. P. Gao, F. T. Chen, Z. Liu and Y. Q. Dai, *Chem. Eng. J.*, 2013, **219**, 478–485.
52 Y. K. Zhang, Z. L. Jin, H. Yuan, G. R. Wang and B. Z. Ma, *Appl. Surf. Sci.*, 2018, **462**, 213–225.
53 M. Khzouz, J. Wood, B. Pollet and W. Bujalski, *Int. J. Hydrog. Energy*, 2013, **38**, 1664–1675.
54 J. C. Lu, X. F. Li, S. F. He, C. Y. Han, G. P. Wan, Y. Q. Lei, R. Chen, P. Liu, K. Z. Chen, L. Zhang and Y. M. Luo, *Int. J. Hydrog. Energy*, 2017, **42**, 3647–3657.
55 P. Tahay, Y. Khani, M. Jabari, F. Bahadoran and N. Safari, *Appl. Catal., A*, 2018, **554**, 44–53.
56 S. Eaimsumang, P. Prataksanon, S. Pongstabodee and A. Luengnaruemitchai, *Res. Chem. Intermed.*, 2020, **46**, 1235–1254.
57 J. Chutirat, S. Eaimsumang and A. Luengnaruemitchai, *Adv. Powder Technol.*, 2020, **31**, 4731–4742.
58 R. Perez-Hernandez, A. D. Avendano, E. Rubio and V. Rodriguez-Lugo, *Top. Catal.*, 2011, **54**, 572–578.
59 M. L. Ang, J. T. Miller, Y. Cui, L. Mo and S. Kawi, *Catal. Sci. Technol.*, 2016, **6**, 3394–3409.
60 C. Herrera, M. Cortés-Reyes, M. Á. Larrubia, M. V. Domínguez-Barroso, M. R. Díaz-Rey and L. J. Alemany, *Appl. Catal., A*, 2019, **582**, 117088.
61 X. Y. Li, L. Li, J. Lin, B. T. Qiao, X. F. Yang, A. Q. Wang and X. D. Wang, *J. Phys. Chem. C*, 2018, **122**, 12395–12403.
62 S. Y. Huang, X. F. Zhu, B. Cheng, J. G. Yu and C. J. Jiang, *Environ. Sci.: Nano*, 2017, **4**, 2215–2224.
63 Y. Y. Wang, C. J. Jiang, Y. Le, B. Cheng and J. G. Yu, *Chem. Eng. J.*, 2019, **365**, 378–388.
64 C. Choong, Z. Y. Zhong, L. Huang, A. Borgna, L. Hong, L. W. Chen and J. Y. Lin, *ACS Catal.*, 2014, **4**, 2359–2363.

© 2023 The Author(s). Published by the Royal Society of Chemistry